Uncertainty estimation in wave energy systems with applications in robust energy maximising control

Mahdiyeh Farajvand [a],[*], Valerio Grazioso [b], Demián García-Violini [a],[c],[d], John V. Ringwood [a]

[a] *Centre for Ocean Energy Research, Maynooth University, Maynooth, Co. Kildare, Ireland*
[b] *Siemens Digital Industrial Software, Interleuvenlaan 68, 3001 Leuven, Belgium*
[c] *Departamento de Ciencia y Tecnología, Universidad Nacional de Quilmes, Roque Saenz Peña 352, Bernal B1876, Argentina*
[d] *Consejo Nacional de Investigaciones Científicas y Técnicas (CONICET), Argentina*

ARTICLE INFO

ABSTRACT

Under control action, wave energy devices typically display nonlinear hydrodynamic behaviour, making the design of energy maximising control somewhat onerous. One solution to approach the optimal performance for nonlinear control problem under model mismatches is to employ a linear control strategy, which can be robust to linear model mismatches. However, accurate characterisation of the uncertainty in the linear model is vital, if the controller is to adequately capture the full extent of the uncertainty, while not being overly conservative due to overestimation of the uncertainty. This paper describes a procedure, employing CFD-based numerical tank experiments, to accurately produce a nominal linear empirical transfer function model, along with an accurate estimate of the uncertainty bounds in that linear model, due to hydrodynamic uncertainty. A robust control case study is provided, illustrating the nominal model estimation process, and its corresponding uncertainty set, including the complete procedure, required to generate the robust controller. Robust control results, on the fully nonlinear CFD model, are provided to demonstrate the efficacy of the modelling and control philosophy.

1. Introduction

Electrification, based on renewables, is a key solution to cater for increasing energy demand and tackle climate change. Among the renewable energy modalities, the exploitation of energy from the ocean waves, due to their high power density and relatively untapped potential, is key. However, economic competitiveness of wave energy converters (WECs) needs to be improved, in which energy-maximising control systems can play an important role.

Model-based control systems contribute to the majority of WEC control strategies, where the system model has a significant influence on the control efficiency. WECs are commonly modelled considering linearity assumptions, i.e. small displacements, based on Cummin's equation [1], with linearised hydrodynamic coefficients. However, linear models, under the linearising assumption of small movements, are challenged due to the requirement for exaggerated device oscillations to maximise power absorption [2]. Thus, the WEC models capturing possible nonlinearities, such as viscous drag, flow separation, vortex shedding [2], power take-off (PTO) nonlinearities [3], and complex

hydrodynamic interactions, should be considered for the design and implementation of model-based control approaches. Nonlinear hydrodynamic modelling of WECs have been reviewed in [4–6]. Among nonlinear WEC models, computational fluid dynamics (CFD)-based numerical wave tanks (NWTs), capturing relevant hydrodynamic non-linearities, have proven to of high-fidelity in research and development [2,7].

A considerable number of energy maximising control approaches have been developed to deal with nonlinear WEC models. Nonlinear model predictive control (NMPC) is a popular model-based control strategy, which obtains an optimal control input (in theory), while handling motion and force constraints systematically over a finite future time horizon [8–10]. Moment-Based nonlinear optimal control, subjected to nonlinear dynamics of the WECs, is another particular energy-maximising strategy, using model order reduction theory by matching the frequency response of the device at specific spectral components (discrete frequencies) [11,12]. Pseudospectral (PS)-based methods are another class of nonlinear WEC control methodology where the continuous-time energy maximisation problem is transcribed into a finite-dimensional optimisation problem. Application of the PS

---

method for a nonlinear WEC control dealing with viscous drag and PTO nonlinearity is reviewed in [13].

Despite the development of different nonlinear control methodologies for WECs, the computational burden of the optimisation problems is a significative aspect [8,14]. In addition, even fully nonlinear WEC models obtained from CFD simulations include numerical errors and uncertainty [15]. To enhance the computational complexity of nonlinear WEC controllers, while improving controller efficiency by dealing with distinct sources of nondeterminism in the WEC model, a robust control methodology, based on a linear nominal WEC model and uncertainty bound, has been developed in [16]. Precise nominal models and small uncertainty bounds are the key roles to reduce conservatism in the robust control design of WECs. Recent efforts have been aimed at accurately characterising the nominal and uncertainty models based on CFD simulations for the optimal robust control design of WECs [17]. However, a particularly important issue of the potential non-passive representation of the nominal and uncertainty model arises from CNWT modelling, which inherently discards intrinsic valuable information and degrades power absorption [17]. In order to best support robust control objectives, there is motivation for passivising a system by means of different approaches, most notably, feedback passivity, practical passivity, and frequency domain passivisation methodology [18]. A recent practical passivisation methodology, proposed by García et al. [19], can be considered for an efficient application of the robust spectral-based control methodology [16], when the system nominal description, or the corresponding uncertainty bounds, violate the intrinsic physical passivity of the system.

In the field of WECs, uncertainty quantification has been addressed in different studies. To briefly summarise, in [20] uncertainty in wave and environmental conditions is quantified and parameterised with the objective of minimising uncertainty towards the impact on power and mooring line tension prediction. Numerical uncertainty estimation for passive control of WECs, focusing on the spatial and temporal discretisation of CFD simulation, is studied Wang et al. [15]. Online estimation of dynamic uncertainty, for robust adaptive optimal control of WECs, is presented in [21]. Recently, a generalised polynomial chaos (gPC) methodology has been utilised for uncertainty estimation, where the studies in [22,23] address the gPC in WEC applications.

Consistent across all the noted studies is the implicit understanding that the fidelity of nominal and uncertainty models plays a crucial role in the effective robust control design for WECs. However, in wave energy robust control, none of the studies to date includes a comprehensive representation of input signal synthesis and characterisation, to give sufficient fidelity in CFD-based NWT tests, for a sensible representation of a nominal model and minimised uncertainty region, while satisfying the passivity condition with the goal of robust control design. Within this context, the latter is tackled in this study, representing a novel and original contribution to the state-of-the-art.

The layout of the remainder of this paper is as follows: First, the CFD-based numerical wave tank setup for system identification and wave excitation force tests, as well as CFD mesh refinement of the set-up, is presented in Section 2. Section 3 details input signal synthesis, including empirical transfer function estimate (ETFE) definition and details on the three types of input signals considered for system identification. Next, data post-processing, related to each input signal type and determination of the best input signal choice for robust model-based control design of the WEC, is presented in Section 4. In Section 5, nominal model determination and uncertainty quantification from ETFE with consideration of ETFE refinement, and ETFE interpolation methodology is presented. A robust control design procedure, with a focus on the input signal required for the control design, is presented in Section 6. Section 7 demonstrates the application example, working through determination of the nominal model, uncertainty region, and robust control design for the case study. The results are presented in Section 7.3 and, finally, conclusions on the overall application are drawn in Section 8.

2. CFD model construction

CFD-based numerical wave tanks (CNWTs), offering complete nonlinear hydrodynamic models, are important tools for analysing WECs. The interaction of the waves and a submerged WEC can be simulated using well-established numerical tools, such as the open-source CFD toolbox OpenFOAM [24], where the fluid behaviour is analysed by numerically solving the Navier–Stokes equations. Under the assumption of incompressible fluid, Reynolds averaged Navier–Stokes (RANS) equations, describing the conservation of mass and momentum, can be written as:

$$\frac{\partial \rho(t,x)}{\partial t} + \nabla.(\rho(t,x)U(t,x)) = 0, \tag{1}$$

$$\frac{\partial \rho(t,x)U(t,x)}{\partial t} + \nabla.\rho U(t,x)U(t,x) = -\nabla p(t,x) + \nabla.(\mu \nabla U(t,x))$$
$$+ \rho f_b(t,x) + f_u(t,x), \tag{2}$$

where Eqs. (1) and (2) represent the conservation equations for mass and momentum, respectively, with t and x denoting the time and spatial variables, respectively, $U(t,x)$ the fluid velocity field, $p(t,x)$ the fluid pressure, ρ the fluid density, μ the dynamic viscosity, and $f_b(t,x)$ the field of external forces, such as gravity.

2.1. NWT configurations

CFD-based NWTs, depending on the modelling objectives, can be designed and equipped in different ways. In this study, two 3D NWT configurations are proposed, based on two different experiment types, i.e. system identification and evaluation tests. The WEC structure with a single degree of freedom, in the heave direction, is considered in our NWT.

2.1.1. NWT for system identification

The three-dimensional CFD-based NWT for system identification tests is designed in a tank with equal span in the x and y-directions, perpendicular to the tank depth (z-direction), with the buoy located in the centre of the tank corresponding to $(x,y,z) = (0,0,0)$. The tank is equipped with a wave absorber at the left and right boundaries ($x = \pm L_{T1}/2$). In the system identification tests, the WEC is driven into motion by applying a defined input force (excitation signal) $f_u(t)$ directly to the WEC, which are notionally applied through the PTO system ($f_u(t)$ is the actual force generated by the PTO). Due to symmetry in both x- and y-directions, the NWT configuration allows the CFD simulation to be carried out on a *quarter of the full NWT*, with a significant advantage in terms of computation time. The side view of the NWT schematic for system identification tests is shown in Fig. 1(a), where D and d are the tank and water depths, respectively, and L_{T1} is the tank length.

For the numerical experiments analysed in this study, the NWT setup is designed in a 6 m deep tank with a water depth of 3 m. The NWT for system identification spanning a length of $L_{T1} = 14$m in the x-direction and 14 m in the y–direction, which is designed to be six wavelengths of the most significant radiated waves (occurring at peak frequency of the radiation damping of the WEC).

2.1.2. NWT for evaluation tests

The three-dimensional CFD-based NWT, for evaluation tests, is designed in a tank spanning the x (wave propagation direction) and y-directions, perpendicular to the tank depth (z-direction), and the buoy's location corresponding to $(x,y,z) = (0,0,0)$. The tank is equipped with a wave generation mechanism (at $x = -c$) and a wave absorber at the down-wave domain boundary (at $x = L_{T2} - c$) specified in [2], where incoming waves alone induce the WEC motion. The side view of the NWT schematic for evaluation tests is shown in Fig. 1(b), where L_{T2} is the tank length, and c is the buoy distance from the wave
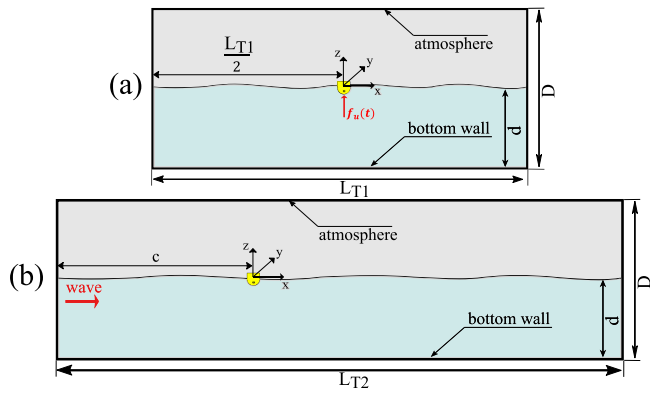
Fig. 1. Schematic of the numerical wave tank for (a) system identification tests and (b) evaluation tests: Side view.
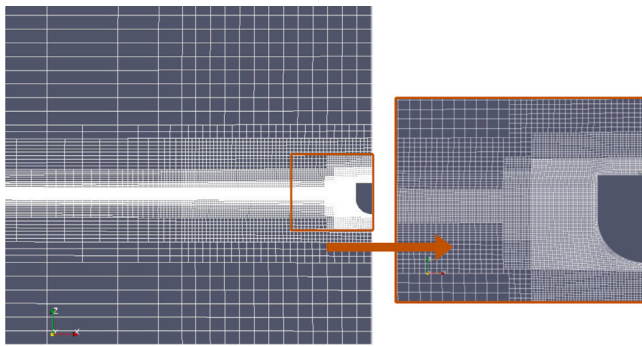

Fig. 2. Paraview snapshots of computational mesh of geometry.

generation boundary. The NWT configuration is symmetric in the y-direction, allowing *a half of the full NWT* for the CFD simulation, which is computationally efficient.

The NWT, for evaluation tests, spans a length of $L_{T2} = 21.1$m in x-direction and 15.6 m in the y-directions, and the buoy location is $c = 7.2$m down-wave (at least one wavelength distance) from the wave generation boundary, and $L_{T2} - c = 13.9$m from wave absorption boundary (at least two wavelengths distance).

2.2. CFD mesh refinement

The spatial discretisation of the NWT is implemented via a mesh; based on the CNWT setup presented in [2], ensuring the efficient and accurate simulations. With the aim of reducing the potential numerical uncertainty effects, additional mesh refinement of the NWT geometry, for system identification tests, is performed to ensure high fidelity. The buoy displacement resulting from the smallest input force is considered to generate the smallest mesh size around the buoy. Meshes are denser around the buoy boundary and gradually increase in size towards the NWT boundary. Mesh refinement is performed on the existing mesh generated in [2,17] by adding more cells and, therefore, decreasing the dimension of the cells around the buoy. Fig. 2 shows a snapshot of the computational mesh of the side view of the quarter NWT using ParaView, an open-source software utility for visualising the data from OpenFOAM. As a result of mesh refinement, the total number of cells increases from the initial number of 1.3 million to 4.06 million, and the cell dimension around the buoy has reduced from 0.013 m to 0.0054 m.

3. Input signal synthesis

Frequency response analysis (FRA) of systems, defined as the ratio of the Fourier transform of the output response to the Fourier

transform of the input excitation, is a well-researched area which is used to characterise the system. In this study, based on well-known optimal conditions for the maximisation of energy absorption [25], the so-called *force-to-velocity* mapping is computed from the set of input excitation forces (PTO force), and their corresponding outputs (velocity) to identify the system. The specification of the system input is one important issue in system identification. The input signal must excite the system over the frequency range where the system has a significant frequency response, while, at the same time, covers the full input amplitude (dynamical) range. Three input signal types and their FRA are considered for this study: Sinusoidal signals, chirp signals, and multisine signals. In order to effectively describe the type of calculation required for the analysis and the use of the input signal, we begin with a definition of the empirical transfer function estimate (ETFE).

3.1. EFTE definition

The linear control design model for the current study is identified via a frequency-domain black-box-identification methodology, aiming to characterise the *force-to-velocity* mapping, i.e. the mapping $f(t) \to v(t)$, where $(f(t), v(t))$ is the input–output pair, defined in the time-domain. By defining $F(j\omega)$ and $V(j\omega)$ as the Fourier transform of the $f(t)$ and $v(t)$, respectively, the ETFE, $H(j\omega)$, is computed as:

$$H(j\omega) = \frac{V(j\omega)}{F(j\omega)}. \tag{3}$$

3.2. Sinusoidal signals

A sinusoidal input, with a single frequency, can be represented by:

$$x(t) = A\sin(\omega t + \phi), \qquad \text{for } t \geq 0, \tag{4}$$

where A, ω, and ϕ are the amplitude, frequency and phase of the sinusoid, respectively. To obtain a complete frequency domain characterisation of the system, for each considered amplitude, 'sufficient'[1] frequency values, ω, should be selected for the system identification tests, as follows: Asymptotic frequency values (low and high frequency limits), as well as the resonance frequency of the device, are of paramount importance. Considering the high variability of the frequency response around the resonance frequency of the system, selection of frequency points around the resonance frequency is advantageous in terms of efficiently capturing the main dynamical behaviour of the system in spectral domain. Using a series of sinusoids as input signal generates a line-spectral characterisation of the system, with a large experimentation time (with sufficient individual sinusoids) to cover the required frequency range.

3.3. Chirp signals

A chirp signal is a signal with a time-varying frequency. Due to the possibility of defining a so-called *instantaneous frequency*, chirp signals are of particular interest. Assigning a specific frequency to every time point in the input signal allows for a one-to-one mapping between time and frequency domains for linear systems.

3.3.1. Linear frequency modulated chirp signal
In a linear frequency modulated (LFM) chirp signal, the instantaneous frequency $f(t)$ varies linearly with time:

$$f(t) = ct + f_0 \tag{5}$$

where f_0 is the initial frequency and c is the chirp rate. A chirp signal in which the frequency *increases* with time is termed 'up-chirp' ($c > 0$ for LFM up-chirp), and a chirp signal in which the frequency *decreases* with time is termed 'down-chirp' ($c < 0$ for LFM down-chirp).

---

[1] According to the specified target spectral discretisation.

The corresponding time-domain function for a sinusoidal linear chirp can be formulated as:

$$x(t) = A\sin\left(\phi_0 + 2\pi\left(\frac{c}{2}t^2 + f_0 t\right)\right), \quad \text{for } t \geq 0, \tag{6}$$

where, A and ϕ_0 are the amplitude and initial phase of the LFM chirp signal, respectively. In a standard LFM chirp signal, A is a constant value while, in an amplitude modulated LFM chirp signal, A is a function of time.

3.3.2. Nonlinear frequency modulation chirp

In a nonlinear frequency modulated (NLFM) chirp signal, the instantaneous frequency $f(t)$ varies nonlinearly with time. A NLFM chirp signal can be defined, for example, by assigning equal, or balanced, permanency time to each frequency where the instantaneous frequency $f(t)$ is calculated as:

$$f(t) = \frac{c}{t} + f_0 \tag{7}$$

3.4. Multisine signals

Multisine signals consist of a sum of several simultaneously generated sinusoids, denoted as:

$$x(t) = \sum_{k=1}^{N} A_k \sin\left(\omega_k t + \phi_k\right), \tag{8}$$

where A_k is the amplitude and ϕ_k the phase of the kth sinusoid, with N the number of sinusoidal components. $\omega_k = \omega_0 + (k-1)\Delta\omega$ is defined for harmonic multisine signals, where ω_0 is the initial frequency and $\Delta\omega$ the constant frequency interval. ω_k, for non-harmonic multisines, is based on user selected frequency points. While A_k and ω_k are normally not chosen independently, in the case of present study we use an open choice on the combination of A_k and ω_k.

Combining sinusoids increases the signal amplitude, which is generally undesirable in NWT experiments, where specific amplitude excitation is desired. In order to produce a specific amplitude multisine, the crest factor (CF), i.e. the ratio of the peak value of a signal to its root mean square level, should be minimised. A well-known frequency-domain CF minimisation methodology, for uniformly spaced frequency components, is Schroeder's method [26], which optimises the ϕ_k to minimise the CF.

4. Data postprocessing

Typically, the NWT output signals show a level of distortion, adversely affecting the system identification process. The primary source of distortion relate to issues associated with limitations of the NWT itself. Most notably, the limitation in NWT length causes wave reflection, and, due to the computational burden, there is also a limitation in the time duration of the excitation signal. A level of post-processing is therefore carried out to mitigate the resulting distortion. A sample CFD-based input/output time domain analysis, based on an input signal with a maximum force amplitude of 20N and signal duration of 25s is considered, to illustrate the post-processing methodology.

4.1. Sinusoidal signal

Sinusoidal CFD-based NWT experiments for the system identification are processed in the time domain data for specific frequency points in the frequency range. Output signal distortion, corresponding to low-frequency input sinusoidal signals, are particularly noticeable, resulting from short signal duration. A potential methodology to reduce such distortion involves the application of a band pass filter (BPF) which passes only frequencies within a specific (narrow) frequency range. The
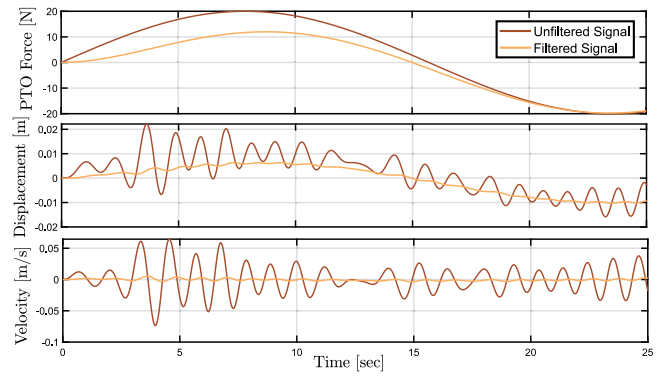

Fig. 3. Time trace of unfiltered and filtered input/output signals for input sinusoidal signal.
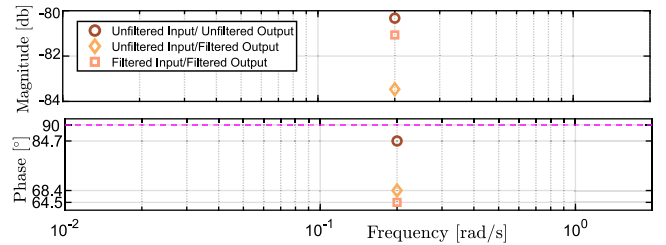

Fig. 4. ETFE for sinusoidal input force.

transfer function of a second-order BPF is formulated from the standard continuous-time form:

$$T_{BP}(s) = G_o \cdot \frac{\left(\frac{\omega_o}{Q_p}\right)s}{s^2 + \left(\frac{\omega_o}{Q}\right)s + \omega_o^2} \tag{9}$$

where G_o is the filter gain, ω_o the centre frequency of the filter, and Q the quality factor, determining the sharpness of the resonance in the filter frequency response. The filter bandwidth, defined as the difference between the higher and lower 3 dB cut-off frequencies, is inversely proportional to Q. A bandpass filter, with a centre frequency of exactly the same frequency as the sinusoidal signal, is employed. To work with the sampled signals, a discrete-time version of the filter is obtained using a matched z-Transform equivalent, with zero initial conditions, and is applied to both input and output signals. Fig. 3 shows sample unfiltered and filtered (using the BPF) input/output time-domain signals from a CFD simulation. The input signal is a single sinusoid with an amplitude of 20N and frequency of 0.2rad/s (low frequency asymptote), and sampling period of 0.001s, over the time interval of [0, 25]s. A direct consequence of the short signal duration is the incomplete period of the signal in this specific case. Considering sinusoidal signals, the ETFE for three different cases, including unfiltered input/unfiltered output, unfiltered input/filtered output, and filtered input/filtered output is computed, with results shown in Fig. 4. The discrete (in both time and frequency) ETFE is obtained using the Fast Fourier transform (FFT), with zero-padding to bring the number of calculation points to the next 2^j (j an integer), as required by the FFT. Based on the phase plot in Fig. 4, applying the BPF to the output signal, or input and output signals for the system identification process, results in even more distortion as the phases diverge from the expected (due to the passive nature of the device) value of 90° at the low frequency asymptote. As a result, BPF was abandoned as a post-processing technique for input/output time domain data using sinusoidal input force experiments.
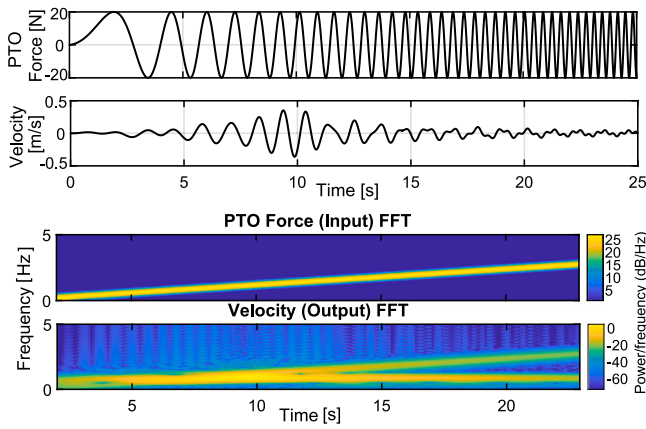
Fig. 5. Time trace and spectrogram of the input/output signals for input LFM up-chirp signal (unfiltered).

4.2. Chirp signal

Chirp CNWT experiments for system identification are simulated at different amplitude levels. Fig. 5 shows the input/output time-domain signals and their corresponding spectrograms. Based on the output spectrogram analysis in Fig. 5, distortion is evident, with the presence of parasitic low-frequency components. One possibility, to diminish this distortion, involves the application of a frequency-varying BPF, where the centre frequency of the filter varies with the instantaneous frequency of the chirp. The transfer function of the frequency-varying second-order BPF can be formulated as in (9), where ω is the time-varying frequency of the filter.

Fig. 6 shows sample unfiltered and filtered input/output time-domain signal from the CFD simulation using a frequency-varying BPF. The input signal is a linear (frequency with time) up-chirp with maximum amplitude of 20N, where the frequency is linearly varying from 0.06rad/s to 18.89rad/s over a time interval of [0, 25]s, with a sampling period of 0.001s. The bandpass filter, with the centre frequency coincident with the signal frequency, is again discretised using a matched z-Transform equivalent and applied to both input and output signals. The ETFE for three different cases, including unfiltered input/unfiltered output, unfiltered input/filtered output, and filtered input/filtered output is computed, and results are shown in Fig. 7. Based on the phase plot in the ETFE, applying the BPF to the output signal, or input and output signals, for the system identification process, results in even more distortion as the phases diverge from the expected value of 90° at the low-frequency asymptote. As a result, BPF was abandoned as a post-processing technique using chirp input force experiments.

4.3. Final choice of input signal

In this section, the potential signal types and their corresponding ETFEs will be examined to choose the best set of input signals for system identification, leading to the most effective control of the WEC. Smaller ETFE variance values, resulting in a correspondingly small uncertainty bound, will lead to the less conservative control of WEC with corresponding improvement in control performance over the full operational space [16]. For comparison, five input signals, and their corresponding ETFEs, are presented in Fig. 8 and Fig. 9, respectively. The time-domain simulations are performed over the interval [0, 25]s. Fig. 8(a) shows a LFM up-chirp signal, specified in Section 3.3.1. Fig. 8(b) shows an amplitude-modulated LFM up-chirp signal (Section 3.3.1), which is obtained by multiplying the LFM up-chirp signal in Fig. 8(a) by the half parabola starting from the value of 7.5 at $t = 0$s and finishing with the value of 1 at
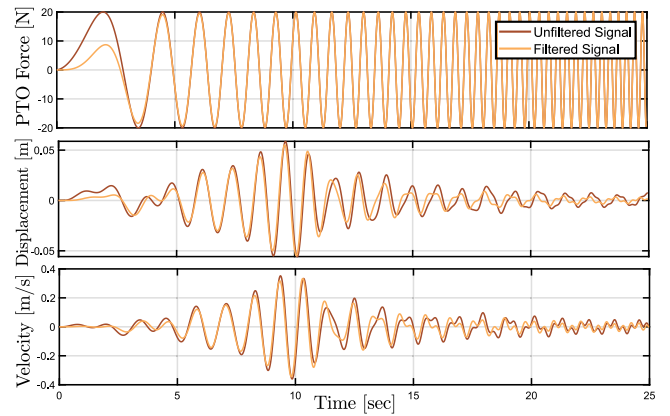

Fig. 6. Time trace of unfiltered and filtered input/output signals based on LFM up-chirp input force.
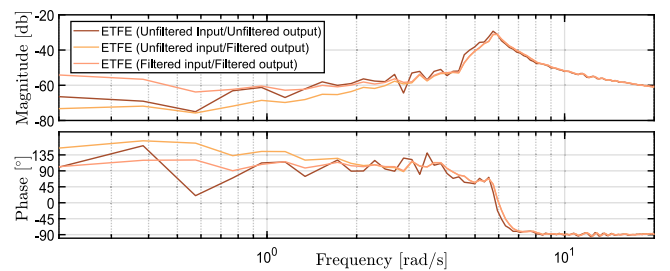

Fig. 7. ETFEs computed from unfiltered input/unfiltered output, unfiltered input/filtered output, and filtered input/filtered output based on LFM up-chirp input force.

resonance time $t = 7.65$s. The NLFM down-chirp signal (Section 3.3.2), with maximum amplitude of 20N, and frequency function according to Eq. (7), which varies from 18.89rad/s to 0.06rad/s, is shown in Fig. 8(c). A sample of a sinusoidal signal (Section 3.2) with an amplitude of 20N and frequency of 5.7rad/s is shown in Fig. 8(d), and finally, the non-harmonic multisine signal (Section 3.4), defined with flat amplitude spectra of 20N and the frequency set of $\Omega = \{0.2, 1, 2, 3, 4, 5, 5.5, 5.7, 6, 6.5, 7, 8, 9, 10, 18.89\}$rad/s and CF optimised using Schroeder's method [26] is presented in Fig. 8(e). The ETFEs, calculated from the various input/output time-domain signals, is presented in Fig. 9. The ETFEs obtained from LFM up-chirp, amplitude-modulated LFM up-chirp, and NLFM down-chirp input signals are shown in red, yellow, and orange lines, respectively. The individual circular and diamond markers represent the ETFE calculated from single sinusoidal signals and the multisine signal with frequencies contained in Ω, respectively.

Based on the ETFEs obtained for the five different input signal types (Fig. 9), the following conclusions can be drawn:

- The ETFE from the LFM up-chirp input signal has high variability, both in magnitude and phase. The main issue arises from the limitation of the simulation time length, which is designed to avoid wave reflections from the tank and also to reduce the computational complexity of the simulations. The limited-time length results in a very short effective time duration spent at each frequency. LFM up-chirp input signals clearly result in considerable phase values above 90° violating the passivity requirement [17].
- The ETFE from the amplitude modulated LFM up-chirp input signal results in a smoother ETFE compared, with the standard linear up-chirp signal, at frequencies up to the resonance frequency of the device, and the overall signal-to-noise ratio is improved. However, passivity issues with this input signal are also evident,
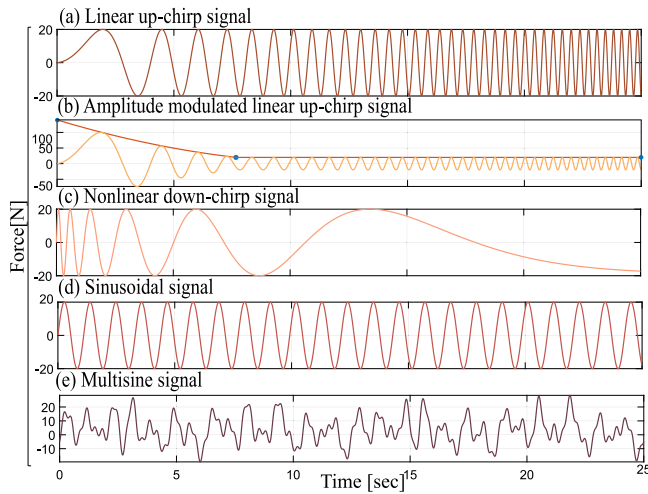
Fig. 8. Time series of potential identification signals.

and the ETFE shows high variability at frequencies higher than the resonance frequency of the device.

- The ETFE from a NLFM down-chirp shows poor resolution and high variability at the resonance frequency and at high frequency, which will result in a large uncertainty bound. However, this experiment results in a relatively good low-frequency asymptote, which is around 90°.
- The ETFE from a non-harmonic multisine signal results in very large variations in the magnitude and phase. One possibility cause may be from distortion of the unequal amounts of time spent at each frequency by the CF optimisation algorithm.
- The ETFE from the sinusoidal input signals is smooth and has low variance, which is a direct result of spending more time at each frequency. This is the best compromise between the 25 s time limit from reflections and the need to spend sufficient time at each frequency to resolve the ETFE.

In summary, the drawbacks associated with the LFM up-chirp, amplitude modulated LFM up-chirp, NLFM down-chirp signals reduce the value of their use in a system identification context. Ultimately, consistent amplitude sinusoidal signals at specific frequency set plus an additional frequency point at resonance were used to excite the system, repeated for different amplitude levels. However, some data from other experiment types, e.g. asymptotic values, are valuable in overall calibration of the data. As a result, these signal characteristics are considered to be a good compromise between time domain data resolution and computational requirements.

In the following, CFD simulations with sinusoidal input types will be exclusively adopted for ETFE calculation.

5. Uncertainty quantification using the EFTE

ETFEs obtained from the CNWT experiments are now used to select both the nominal model and quantify the uncertainty for robust control design. ETFE refinement is performed prior to nominal and uncertainty model selection to ensure the correct asymptotic nature of the ETFE and passivity of the WEC model. Ultimately, the total uncertainty measured is a combination of nonlinearity in the (linear) nominal model, together with some minor phenomena resulting from imperfect simulation in the NWT.

5.1. EFTE refinement

ETFE refinement refers to mitigation of ETFE distortion arising from the CNWT experimental errors. ETFE refinement is carried out based on the satisfaction of two fundamental physical properties of the system:

5.1.1. Asymptotic nature of the ETFE

In order to ensure asymptotic behaviour consistent with a passive system, the ETFE phase components are forced to 90° and −90° at the low and high-frequency asymptotes, respectively.

5.1.2. Passive nature of the WEC

Considering the passive behaviour, which is formulated based on physical energy processes of the device, a passivisation methodology, based on Bode plot shaping, is applied. In this study, ETFE refinement is performed by means of forcing the phase within ±90° degrees *for all frequencies*.

5.2. Uncertainty quantification

The methodology for determining the nominal model and specifying uncertainty, based on the ETFEs calculated from the NWT experimental data, is presented in this section.

5.2.1. Nominal model determination

The nominal model, based on the calculated ETFEs, can be determined using different approaches. Three possible choices are:

1. *Nominal model based on average ETFE:* In this methodology, the nominal model is calculated by taking the average of all ETFEs.
2. *Nominal model based on the most linear case:* This approach uses the ETFE corresponding to the smallest input force amplitude. The nominal model based on the smallest force will result in the closest model calculated by linear boundary element methods (BEMs) [27]. However, nominal model selection based on a linear approach may result in a large uncertainty region, with resulting conservative control [17].
3. *Nominal model based on minimum radius circles:* This method produces synthetically built nominal model, which is formulated to minimise the uncertainty region. At each frequency point, the nominal model is located at the centre of a minimum radius circle which includes the extremities of the uncertainty region [16,17].

5.2.2. Uncertainty specification

The uncertainty region, at a specific frequency point, is calculated based on the minimum distance between the nominal model and experimental models of different amplitude levels at that frequency. The multiplicative uncertainty, $\Delta_m(\omega)$, is defined :

$$\max_{1 \leqslant i \leqslant n} \{|\Delta_m^i(\omega)|\} = \max_{1 \leqslant i \leqslant n} \left\{ \left| \frac{H^i(\omega) - G_o(\omega)}{G_o(\omega)} \right| \right\} \tag{10}$$

where *n* is the number of experiment sets and G_o is the nominal model.

5.3. ETFE interpolation

Since the number of frequency points returned in the ETFE is limited by the number of individual sinusoids used for excitation (16 points), some level of interpolation is required to provide an adequate number of frequency points for robust control design. This is due to the pseudospectral nature of the control design, where a number of pseudospectral *basis functions* considerably in excess of 16 is required. Such an interpolation can be carried out using two methods: *(A)* Interpolation of the ETFEs based on the basis function frequency points and determination of the nominal model and uncertainty bounds at these points *OR (B)* Determination of the nominal model and uncertainty bounds from the raw ETFEs *and then interpolate* the nominal model and uncertainty bound at the basis function frequency points. Methodology *(A)* is adopted since, by first interpolating the sinusoidal based ETFEs, smoother interpolation is obtained.
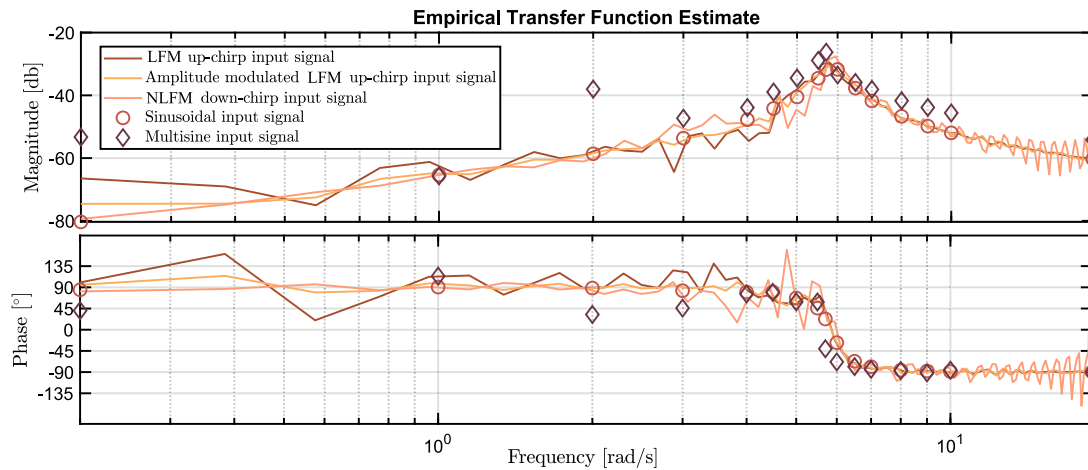
Fig. 9. Empirical transfer function estimate obtained from five different input signals: LFM up-chirp input signal, amplitude modulated LFM up-chirp signal, NLFM down-chirp input signal, sinusoidal input signals, and multisine input signal. Note that the multisine and individual sinusoids are only defined at discrete frequency points.

6. Robust control design

The control objective for the WEC system is to maximise the total absorbed energy, J, defined as:

$$J \equiv E = -\int_0^T P dt = -\int_0^T v^T(t)u(t)dt, \tag{11}$$

which, in spectral and pseudospectral form, can be reformulated as:

$$J \approx J_N = \int_0^T \hat{u}^T \Phi^T(t)\Phi(t)\hat{v} = -\frac{T}{2}\hat{u}^T\hat{v}, \tag{12}$$

In (11) and (12), E represents the absorbed power over the time interval $[0 \quad T]$, P the instantaneous power, $u(t)$ the control force applied through the PTO system, and $v(t)$ the device velocity. $\hat{u}$ and $\hat{v}$ are approximations of $u(t)$ and $v(t)$ using an orthogonal set of basis functions Φ [16]. Substituting the approximation of the equation of motion of the WEC, $\hat{v} = G(\hat{u}+\hat{e})$, into the approximate absorbed energy expression in (12), the following equality is obtained:

$$J_N = -\frac{T}{2}\hat{u}^T G(\hat{u}+\hat{e}), \tag{13}$$

which is a quadratic function in the control variable $\hat{u}$ alone. In (13), G is defined as the system model and $\hat{e}$ is an approximation of the wave excitation force. If the concavity of Eq. (13) can be guaranteed, there will exist a global maximum for the optimisation problem, with optimal solution:

$$\hat{u}_o^\star = -(G+G^T)^{-1}G\hat{e}. \tag{14}$$

The optimal value of J_N, with (14) is substituted into (12), is then

$$J_N^\star = \frac{T}{2}\hat{u}_o^{\star T} G(\hat{u}_o^\star + e). \tag{15}$$

For application of the robust control approach, the system model, G should represent a family of models which includes the nominal plus uncertainty model, defined as:

$$G = G_o + \Delta_a, \tag{16}$$

with G_o representing the nominal model of the system and $\Delta_a \in \mathbb{R}^{N\times N}$ the uncertainty model, formulated as:

$$G_o = \bigoplus_{k=1}^{N/2} \begin{bmatrix} \mathcal{R}_k^o & \mathcal{I}_k^o \\ -\mathcal{I}_k^o & \mathcal{R}_k^o \end{bmatrix} \tag{17}$$

and

$$\Delta_a = \bigoplus_{k=1}^{N/2} \begin{bmatrix} \delta_k^\mathcal{R} & \delta_k^\mathcal{I} \\ -\delta_k^\mathcal{I} & \delta_k^\mathcal{R} \end{bmatrix}, $$

where

$$\mathcal{R}_k^o = \mathbb{R}e\{g_o(j\omega_k)\}, \mathcal{I}_k^o = \mathbb{I}m\{g_o(j\omega_k)\}$$

and

$$\delta_k^\mathcal{R} = \mathbb{R}e\{\delta_k\}, \delta_k^\mathcal{I} = \mathbb{I}m\{\delta_k\}.$$

$\mathcal{R}_k^o, \mathcal{I}_k^o \in \mathbb{R}$, and $g_o(j\omega_k)$ represent the nominal frequency response, while $\delta_k \in \mathbb{C}$ represents the uncertainty level at frequency ω_k. Considering the feasibility (passivity) condition for the real system, G must be positive real:

$$\mathcal{R}_k = \mathcal{R}_k^o + \delta_k^\mathcal{R} > 0, \tag{18}$$

where $\mathcal{R}_k$ is the real part of the system model.

Using the feasibility condition and defining the bestworst case performance (best-WCP) solution as the input that minimises the performance degradation when the system under study is affected by a bounded uncertainty set Δ, the robust control problem statement can be defined as:

$$\hat{u}_r^\star \leftarrow \max_{\hat{u}\in\mathbb{R}^N} \min_{\Delta\in\mathcal{U}} J_N. \tag{19}$$

Eq. (19) represents a robust quadratic formulation where $\mathcal{U}$ indicates the set of all possible uncertainty.

7. Case study

7.1. System setup

The point absorber-type WEC considered for this study has an axisymmetric cylindrical geometry and hemispherical bottom. A schematic of the structure, including all relevant physical properties, are shown in Fig. 10. The radius of the hemispherical and cylindrical sections is 0.25 m, with the height of the cylindrical section also 0.25 m. The mass of the device is 43.67 kg, with the centre of the mass located at a vertical distance of 0.191 m from the bottom-most point of the buoy.

7.2. ETFE evaluation

The ETFEs resulting from the complete set of sinusoidal exciting signals are shown in Fig. 11. ETFE determination is based on the NWT configuration presented in Section 2.1.1. The sinusoidal PTO force excitation signals consist of a total of 96 experiments combining the amplitude set $A_i = \{20, 40, 60, 80, 100, 120\}$N using a set of individual frequencies $w_j \in \{0.2, 1, 2, 3, 4, 5, 5.5, 5.7, 6, 6.5, 7, 8, 9, 10, 18.89\}$ rad/s plus a resonance frequency specific to each amplitude set. This selection
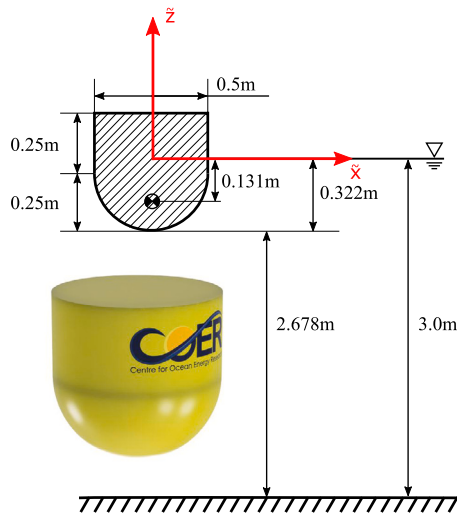
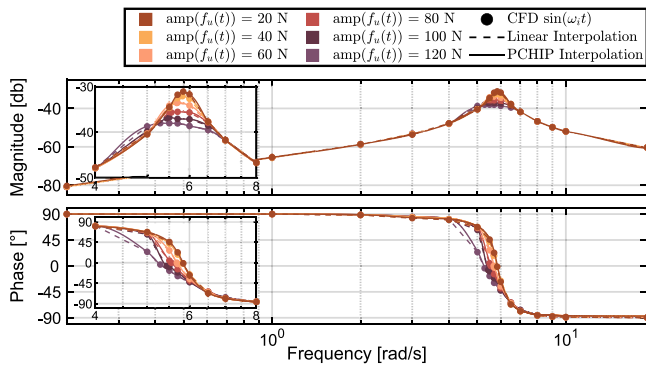**Fig. 10.** Schematic of the considered WEC structure.

Fig. 11. Empirical transfer function estimates (ETFEs) for the 6 amplitude levels, using sinusoidal signal excitation (based on unfiltered data).

of frequencies and amplitudes gives a smooth representation transition between the ETFE points corresponding to discrete values of amplitude/frequency. In particular, the amplitude range selection ranging from linear behaviour (smallest amplitude) to amplitudes forcing the device out of the water (largest amplitude) and intermediate values, covers a full dynamical characterisation of the nonlinear system. Each experiment is driven by a finite set of N exciting force signals that generate a corresponding set of velocity signals. The simulation time of the sinusoidal experiments is the interval $[0, 25]$s. The ETFEs for each of the A_i amplitudes, after the employment of ETFE refinement as explained in Section 5.1, and interpolation across frequency points using piecewise cubic Hermite interpolating polynomials (PCHIPs), are shown in Fig. 11.

In this study, three nominal model candidates are considered for robust control design. Fig. 12 shows the interpolated ETFEs, along with the three nominal model possibilities; $\hat{G}(\omega)$ is the nominal model based on the average ETFE, $G_{lin}(\omega)$ is the nominal model based on a linear BEM approach, and $G_{circ}(\omega)$ is based on the minimum radius uncertainty circles as detailed in Section 5.2.1 (1–3). The same information, including the ETFEs and the three nominal model candidates, is shown in Fig. 13 on a polar (Nyquist) plot.

The uncertainty bound, based on the formulation presented in Section 5.2.2, is obtained for the three nominal model candidates, with results as shown in Fig. 14. Comparing the uncertainty magnitude corresponding to the three different nominal models, $\hat{G}(\omega)$, $G_{lin}(\omega)$, and $G_{circ}(\omega)$, it is clear that selection of the centre of the minimum radius circles as a nominal model ($G_{circ}(\omega)$) results in a significantly smaller
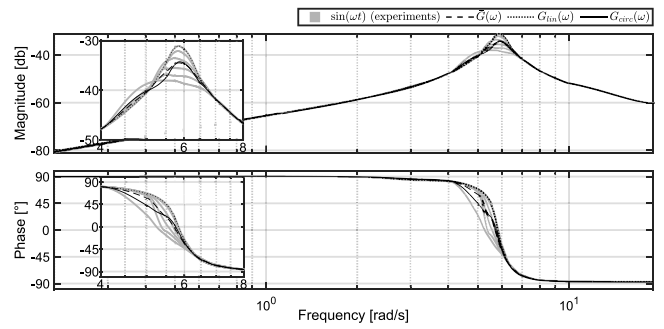

Fig. 12. ETFE and Nominal models based on $\hat{G}(\omega)$, $G_{lin}(\omega)$, and $G_{circ}(\omega)$.
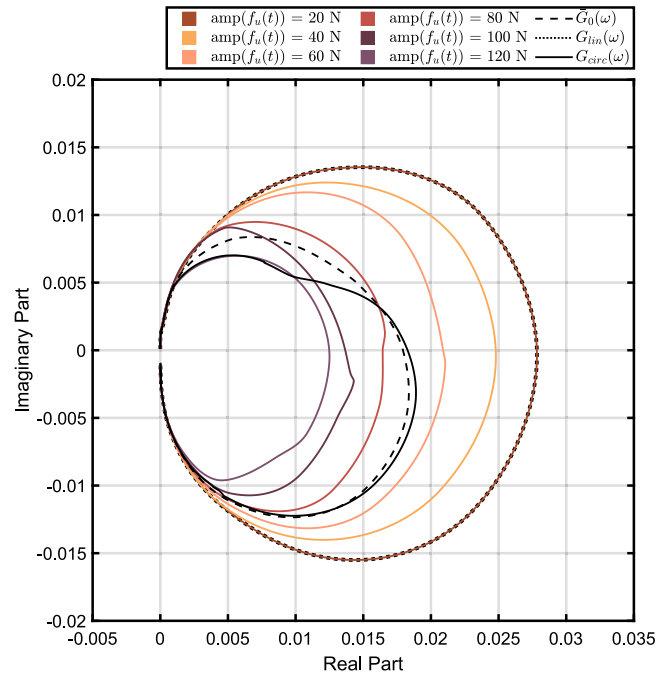

Fig. 13. ETFEs and nominal models based on $\hat{G}(\omega)$, $G_{lin}(\omega)$, and $G_{circ}(\omega)$ in polar form.
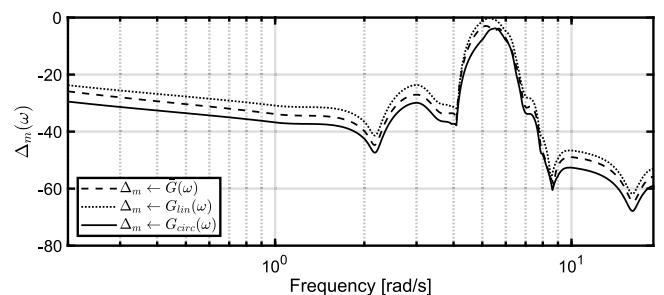

Fig. 14. Uncertainty size $|\varDelta_m|$ using multiplicative uncertainty structure for three different nominal models $\hat{G}(\omega)$, $G_{lin}(\omega)$, and $G_{circ}(\omega)$.

multiplicative uncertainty bound, $|\varDelta_m|$. The ETFEs, the three different nominal models, and their corresponding uncertainty regions are also represented in the Nyquist (polar) domain, shown in Fig. 15.

7.3. Sample robust control results

The control part of this study is based on the assumption of full knowledge of the wave excitation force. Wave excitation force tests are simulated in a CFD environment, as detailed in 2.1.2. The WEC
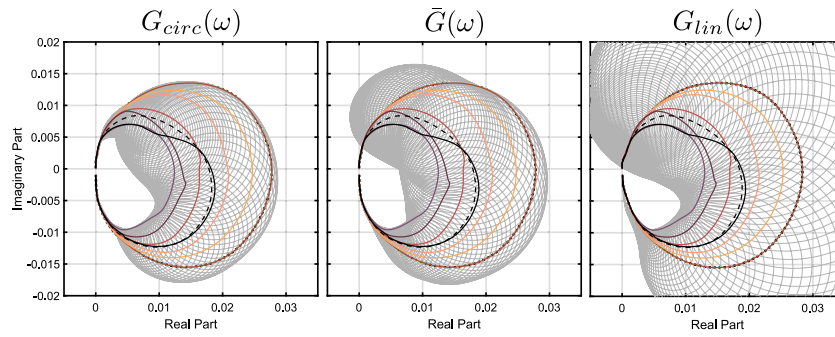
Fig. 15. ETFEs, Nominal models based on $\hat{G}(\omega)$, $G_{lin}(\omega)$, and $G_{circ}(\omega)$, and their corresponding uncertainty, in polar form.
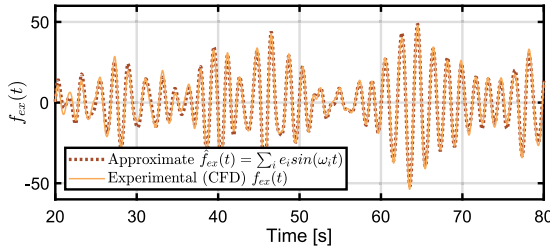

Fig. 16. Experimental and approximated wave excitation force.

Fig. 17. Frequency components of the optimal control inputs.

Fig. 18. Time trace of the absorbed energy, applying different control input forces to the different nominal models.

structure is exposed to the irregular incident waves of a JONSWAP spectrum with a significant wave height of $Hs = 0.1$m, peak period of $T_p = 1.94$s, and steepness parameter $\gamma = 3.3$. This condition represents realistic, scaled conditions at the AMETS test site in Bellmullet, Co. Mayo, off the West Coast of Ireland [28], which has challenging wave conditions, consistent with the generation of nonlinear hydrodynamic fluid/device interaction. (To retain deep water conditions of the AMETS site, the Froude scaling with a scaling factor of 1/30th is applied [29].) The time-domain representation the wave excitation force, extracted from the numerical simulation data, together with the approximated excitation force using 63 frequency components, is shown in Fig. 16. A good agreement between the approximated excitation $\tilde{f}_{ex}(t)$ and experimental excitation wave force $f_{ex}(t)$ can be observed.

The robust controller is designed based on the nominal models, G_{circ} (the nominal model corresponding to the smallest uncertainty size (Fig. 14)) and $G_{test}(\omega)$, where $G_{test}(\omega)$ is a generic test model contained in the family of systems, represented by the set of circular boundaries. In addition, two solutions for the optimal control forces are computed:

- $u_o(t)$ is computed using the nominal approach, i.e. using the nominal model, $G_{circ}(\omega)$.
- $u_r(t)$ is computed using the robust approach, based on experimental test models, $H^i(\omega)$.

The sin and cos frequency component coefficients of the optimal control inputs, $u_o(t)$ and $u_r(t)$ are shown in Fig. 17. Note that, in general, the components corresponding to $u_o(t)$ have a greater amplitude than $u_r(t)$. For assessment of the control performance, the following steps are taken:

1. $u_o(t)$ is applied to $G_{circ}(\omega)$ and $G_{test}(\omega)$, and
2. $u_r(t)$ is applied to $G_{circ}(\omega)$ and $G_{test}(\omega)$.

Fig. 18 shows the time trace of absorbed energy when $u_o(t)$ and $u_r(t)$ are applied to $G_{circ}(\omega)$ and $G_{test}(\omega)$.

- The solid red line represents the absorbed energy when $u_o(t)$ is applied to the nominal model $G_{circ}(\omega)$. This case is the ideal performance, where the optimal control input using nominal model $G_{circ}(\omega)$ is applied to the same nominal system.
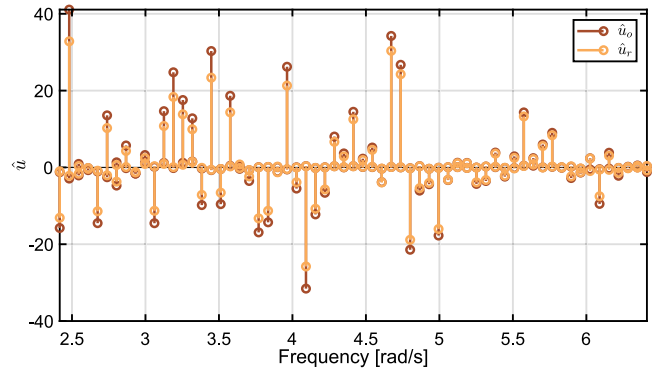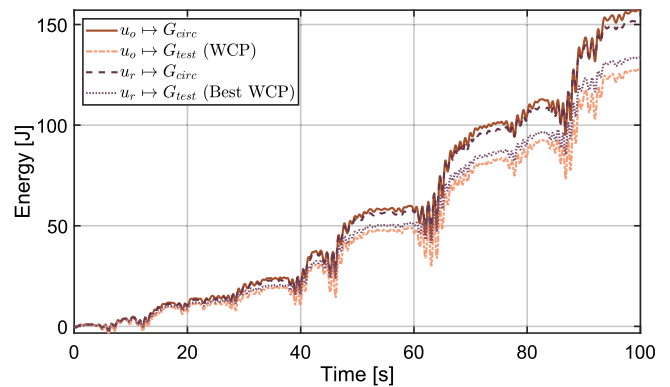
- The orange dashed line represents the absorbed energy when $u_o(t)$ is applied to the nominal model $G_{test}(\omega)$. In particular, as the test model has been specifically selected, this case is the worst performance, where the optimal control input using the nominal model $G_{circ}(\omega)$ is applied to the nominal model $G_{test}(\omega)$.
- The dark purple dashed line represents the absorbed energy when $u_r(t)$ is applied to the nominal model $G_{circ}(\omega)$. In this case, the performance of the system has improved and absorbed energy of the system has moved closer to the absorbed energy for ideal performance.
- The purple dashed line represents the absorbed energy when $u_r(t)$ is applied to the nominal model $G_{test}(\omega)$. This case is the best worse-case performance for energy absorption.

Comparing the results of applying $u_r(t)$ to the two different nominal models, the impact of the correct selection of nominal model and uncertainty bound is highlighted. In robust control, applying $u_r(t)$,

where the nominal model is based on the centre of the minimum radius circles ($G_{circ}(\omega)$), which corresponds to a small size of uncertainty bound, improves the control performance. Fig. 18 shows that the mean generated power, using the robust approach, is always non-negative, which is in accordance with the principle of non-consumption of power using robust approaches. In this study, nominal control also results in a positive mean absorbed energy, but in the general (non-robust) case, negative mean power 'production' can occur, for mismatched control/system models [16].

8. Conclusions

This study proposes a framework for estimating uncertainty in WEC systems with applications in robust control. With the objective of obtaining high-fidelity results from a CFD-based NWT, mesh refinement has been applied to the NWT setup proposed in [17], resulting in improved ETFE resolution considering the same experiments. The main contribution of this study is the synthesis of input signal types, and post-processing towards the aim of reducing conservatism in the WEC uncertainty description with the following results:

- Sinusoidal signals: Computing an ETFE with individual sinusoidal input signals and their corresponding output signals results in a high level of fidelity in terms of a low-variability ETFE, and satisfying the asymptotic nature of the phase response with minor errors which are addressed by applying ETFE refinement. It has been shown that there is no value in applying a BPF for the experiments showing distortion in the output signal. The major drawback for the experiments with individual sinusoidal signals is the high computational cost (relatively long simulation time).
- Chirp signal: The ETFEs obtained from LFM up-chirp input signals, and their corresponding output signals, show high variability, resulting in a large uncertainty region, while distorting the passive nature of the asymptotic ETFE properties. ETFEs obtained from input/output signals by pre-distorting the LFM up-chirp input signal, by modulating the input amplitude, resulted in a less variable ETFE, at low frequency. However, the resulted ETFE, computed from amplitude modulated LFM up-chirp signal, is not as smooth as the ETFE obtained from sinusoidal input signals. Moreover, the ETFE obtained from a NLFM down-chirp resulted in a highly variable ETFE at resonance and at high frequency. It has been shown that application of a BPF to the input/output signals is problematic, due to the difficulty of correct initialisation of the filter output, resulting in unwanted additional transient behaviour artefacts.
- Multisine: ETFEs obtained from non-harmonic multisine signal show high variability. The application of Schroder's minimisation method to a multisine signal, with user selected frequencies, results in a highly-variable ETFE, with distortion of the amount of time spent at each frequency as a likely explanation. Thus, it can be concluded that achieving a balance between minimisation of the crest factor, and concentrating on the particular frequencies (non-harmonic multisine), is virtually impossible.

In the NWT experiments, proper input signal selection, application of ETFE refinement, and quantifying uncertainty by representative nominal model selection and uncertainty region estimation, results in a passive system representation and small uncertainty region, which improves robust control performance. The comparison of the overall energy absorption from this study and [17] highlights the improvement in the resulting controller performance.

CRediT authorship contribution statement

Mahdiyeh Farajvand: Conceptualization, Methodology, Investigation, Formal analysis, Software, Writing – original draft, Writing – review & editing, Visualization. **Valerio Grazioso:** Conceptualization, Methodology, Investigation, Formal analysis, Software. **Demián García-Violini:** Methodology, Formal analysis, Software, Writing – review & editing. **John V. Ringwood:** Conceptualization, Writing – review & editing, Supervision, Funding acquisition, Project administration.

Declaration of competing interest

The authors declare that they have no known competing financial interests or personal relationships that could have appeared to influence the work reported in this paper.

Acknowledgements

References

[1] W.E. Cummins, The impulse response function and ship motions, Schiffstechnik 47 (1962) 101–109.

[2] C. Windt, N. Faedo, M. Penalba, F. Dias, J.V. Ringwood, Reactive control of wave energy devices–the modelling paradox, Appl. Ocean Res. 109 (2021) 102574.

[3] M. Penalba, J.V. Ringwood, A high-fidelity wave-to-wire model for wave energy converters, Renew. Energy 134 (2019) 367–378.

[4] H.A. Wolgamot, C.J. Fitzgerald, Nonlinear hydrodynamic and real fluid effects on wave energy converters, Proc. Inst. Mech. Eng. A 229 (7) (2015) 772–794.

[5] M. Penalba, G. Giorgi, J.V. Ringwood, Mathematical modelling of wave energy converters: A review of nonlinear approaches, Renew. Sustain. Energy Rev. 78 (2017) 1188–1207.

[6] C. Windt, J. Davidson, J.V. Ringwood, High-fidelity numerical modelling of ocean wave energy systems: A review of computational fluid dynamics-based numerical wave tanks, Renew. Sustain. Energy Rev. 93 (2018) 610–630.

[7] C. Windt, N. Faedo, D. García-Violini, Y. Peña-Sanchez, J. Davidson, F. Ferri, J.V. Ringwood, Validation of a CFD-based numerical wave tank model of the 1/20th scale wavestar wave energy converter, Fluids 5 (3) (2020) 112.

[8] N. Faedo, S. Olaya, J.V. Ringwood, Optimal control, MPC and MPC-like algorithms for wave energy systems: An overview, IFAC J. Syst. Control 1 (2017) 37–56.

[9] N. Tom, R.W. Yeung, Nonlinear model predictive control applied to a generic ocean-wave energy extractor, J. Offshore Mech. Arct. Eng. 136 (4) (2014).

[10] M. Richter, M.E. Magana, O. Sawodny, T.K. Brekken, Nonlinear model predictive control of a point absorber wave energy converter, IEEE Trans. Sustain. Energy 4 (1) (2012) 118–126.

[11] N. Faedo, Y. Peña-Sanchez, J.V. Ringwood, Finite-order hydrodynamic model determination for wave energy applications using moment-matching, Ocean Eng. 163 (2018) 251–263.

[12] N. Faedo, G. Scarciotti, A. Astolfi, J.V. Ringwood, Energy-maximising control of wave energy converters using a moment-domain representation, Control Eng. Pract. 81 (2018) 85–96.

[13] G. Bacelli, R. Genest, J.V. Ringwood, Nonlinear control of flap-type wave energy converter with a non-ideal power take-off system, Annu. Rev. Control 40 (2015) 116–126.

[14] A. Mérigaud, J.V. Ringwood, Improving the computational performance of nonlinear pseudospectral control of wave energy converters, IEEE Trans. Sustain. Energy 9 (3) (2017) 1419–1426.

[15] W. Wang, M. Wu, J. Palm, C. Eskilsson, Estimation of numerical uncertainty in computational fluid dynamics simulations of a passively controlled wave energy converter, Proc. Inst. Mech. Eng. M 232 (1) (2018) 71–84.

[16] D. Garcia-Violini, J.V. Ringwood, Energy maximising robust control for spectral and pseudospectral methods with application to wave energy systems, Internat. J. Control 94 (4) (2021) 1102–1113.

[17] M. Farajvand, D. García-Violini, C. Windt, V. Grazioso, J. Ringwood, Quantifying hydrodynamic model uncertainty for robust control of wave energy devices, in: 14th European Wave and Tidal Energy Conference, EWTEC, 2021, pp. 2251–1:2251–10.

[18] E.M. Navarro-López, E. Licéaga-Castro, Combining passivity and classical frequency-domain methods: An insight into decentralised control, Appl. Math. Comput. 215 (12) (2010) 4426–4438.

[19] D. García-Violini, M. Farajvand, C. Windt, V. Grazioso, J.V. Ringwood, Passivity considerations in robust spectral-based controllers for wave energy converters, in: 2021 XIX Workshop on Information Processing and Control, RPIC, IEEE, 2021, pp. 1–6.

[20] B. Robertson, H. Bailey, B. Buckham, Resource assessment parameterization impact on wave energy converter power production and mooring loads, Appl. Energy 244 (2019) 1–15.

[21] J. Na, G. Li, B. Wang, G. Herrmann, S. Zhan, Robust optimal control of wave energy converters based on adaptive dynamic programming, IEEE Trans. Sustain. Energy 10 (2) (2018) 961–970.

[22] G.M. Paredes, C. Eskilsson, J.P. Kofoed, Uncertainty quantification of the dynamics of a wave energy converter, in: MARINE 2019-VIII International Conference on Computational Methods in Marine Engineering, 2019, pp. 157–168.

[23] B. Yildirim, G.E. Karniadakis, Stochastic simulations of ocean waves: An uncertainty quantification study, Ocean Model. 86 (2015) 15–35.

[24] C. DIrect, OpenFOAM, 2022, https://www.openfoam.com/. (Accessed online: 14 June 2022).

[25] J. Falnes, Ocean Waves and Oscillating Systems: Linear Interactions Including Wave-Energy Extraction, Cambridge Univ. Press, 2002.

[26] M. Schroeder, Synthesis of low-peak-factor signals and binary sequences with low autocorrelation (Corresp.), IEEE Trans. Inform. Theory 16 (1) (1970) 85–89.

[27] J. Davidson, S. Giorgi, J.V. Ringwood, Linear parametric hydrodynamic models for ocean wave energy converters identified from numerical wave tank experiments, Ocean Eng. 103 (2015) 31–39.

[28] R. Atan, J. Goggins, S. Nash, A detailed assessment of the wave energy resource at the atlantic marine energy test site, Energies 9 (11) (2016) 967.

[29] V. Heller, Scale effects in physical hydraulic engineering models, J. Hydraul. Res. 49 (3) (2011) 293–306.